Journal of Physics: Condensed Matter

PAPER

Mn substitution in the topological metal Zr_2Te_2P

To cite this article: O Oladehin *et al* 2022 *J. Phys.: Condens. Matter* **34** 485501

IOP Publishing Journal of Physics: Condensed Matter
J. Phys.: Condens. Matter **34** (2022) 485501 (8pp) https://doi.org/10.1088/1361-648X/ac9770

Mn substitution in the topological metal Zr_2Te_2P

O Oladehin[1,2], K Feng[1,2], J W Haddock[4], J Galeano-Cabral[1,3], K Wei[1], Y Xin[1], S E Latturner[4] and R E Baumbach[1,2,*]

[1] National High Magnetic Field Laboratory, Florida State University, Tallahassee, FL 32310, United States of America
[2] Department of Physics, Florida State University, Tallahassee, FL 32306, United States of America
[3] Department of Mechanical Engineering, Florida State University, Tallahassee, FL 32306, United States of America
[4] Department of Chemistry and Biochemistry, Florida State University, Tallahassee, FL 32306, United States of America

E-mail: baumbach@magnet.fsu.edu

Received 18 July 2022, revised 22 September 2022
Accepted for publication 4 October 2022
Published 17 October 2022

Abstract

Results are reported for Mn intercalated Zr_2Te_2P, where x-ray diffraction , energy dispersive spectroscopy, and transmission electron microscopy measurements reveal that the van der Waals bonded Te–Te layers are partially filled by Zr and Mn ions. This leads to the chemical formulas $Zr_{0.07}Zr_2Te_2P$ and $Mn_{0.06}Zr_{0.03}Zr_2Te_2P$ for the parent and substituted compounds, respectively. The impact of the Mn ions is seen in the anisotropic magnetic susceptibility, where Curie–Weiss fits to the data indicate that the Mn ions are in the divalent state. Heat capacity and electrical transport measurements reveal metallic behavior, but the electronic coefficient of the heat capacity ($\gamma_{Mn} \approx 36.6$ mJ (mol·K^2)$^{-1}$) is enhanced by comparison to that of the parent compound. Magnetic ordering is seen at $T_M \approx 4$ K, where heat capacity measurements additionally show that the phase transition is broad, likely due to the disordered Mn distribution. This transition also strongly reduces the electronic scattering seen in the normalized electrical resistance. These results show that Mn substitution simultaneously introduces magnetic interactions and tunes the electronic state, which improves prospects for inducing novel behavior in Zr_2Te_2P and the broader family of ternary tetradymites.

Keywords: topological metal, magnetism, single crystal synthesis

(Some figures may appear in colour only in the online journal)

1. Introduction

Electronic band structure calculations, angle resolved photoelectron spectroscopy (ARPES), scanning tunneling spectroscopy, and quantum oscillation measurements have shown that the tetradymite materials M_2Te_2X (M = Ti, Zr, or Hf and X = P or As) exhibit unusual combinations of conventional and topological electronic bands [1–5]. This includes Dirac points (above the Fermi energy at the Γ-point) and Dirac node arcs (below the Fermi energy at the M-point), where recent spin-ARPES measurements clarified that the Dirac node arcs have nontrivial spin textures for all three of the chemical variants [6]. Under certain conditions these combined features might produce novel electronic states, but here they are hundreds of meV away from the Fermi energy E_F and the electronic properties are dominated by the conventional bands. Thus, it is appealing to search for strategies to move the Fermi

* Author to whom any correspondence should be addressed.

energy into their vicinity. Chemical tuning also has the potential to induce interesting electronic/magnetic states such as magnetic order or superconductivity. Earlier work studying the tetradymite topological insulators $Bi_2(Se,Te)_3$ provides some guidance for how to do this, where chemical intercalation and substitution have been used to produce a variety of behaviors: e.g. Cu and Sr intercalation induce superconductivity [7–12] while other transition metal substitution produces magnetic ordering [13–15]. Chemical tuning using magnetic ions also has the potential to produce intriguing behaviors that result from time reversal symmetry breaking: e.g. where Dirac nodes are split into Weyl points. The presence of magnetic ions could also produce nontrivial magnetoeletric coupling such as a topological Hall effect [16, 17].

This motivated us to focus on chemical tuning in Zr_2Te_2P that might (a) preserve the band structure but change the Fermi energy, (b) introduce interactions between the electrons in the non-trivial bands with other order parameters or (c) introduce other ordered states (e.g. magnetism). An earlier effort was made for Cu_x:Zr_2Te_2P ($x \lesssim 0.1$), showing that chemical tuning is feasible, but the electronic behavior was not substantially modified [1]. $Zr_{2+\delta}Te_2P$ with $0 < \delta < 1.5$ was also previously reported, where the excess Zr ions occupy the weakly bonded layer between the van der Waals bonded Te–Te atoms [18]. Here we introduced Mn into Zr_2Te_2P, which would be expected to introduce magnetism, as well as to result in possible charge tuning. X-ray diffraction (XRD), energy dispersive spectroscopy, and transmission electron microscopy (TEM) measurements show that (a) even for the parent compound, excess Zr ions are present between the Te–Te layers and (b) that the Mn ions are randomly distributed in the same position. Based on these data, we find the chemical formulas $Zr_{0.07}Zr_2Te_2P$ and $Mn_{0.06}Zr_{0.03}Zr_2Te_2P$.

Temperature and magnetic field dependent magnetization, heat capacity, and electrical transport measurements for $Mn_{0.06}Zr_{0.03}Zr_2Te_2P$ reveal significant differences from the parent compound, where local moment magnetism due to divalent Mn is observed. Heat capacity measurements uncover Fermi liquid behavior with a Sommerfeld coefficient $\gamma_{Mn} \approx 36.6\,\mathrm{mJ\,(mol{\cdot}K^2)^{-1}}$ that is enhanced by comparison to the value of the parent compound $\gamma \approx 5.3\,\mathrm{mJ\,(mol{\cdot}K^2)^{-1}}$. At low temperatures the Mn containing specimen exhibits magnetic ordering at $T_M \approx 4\,\mathrm{K}$ with easy *ab*-plane anisotropy, although the broadness of the transition in heat capacity measurements suggests that it is strongly disordered. The ordering also removes magnetic scattering of the conduction electrons, resulting in a decrease of the normalized electrical resistance. While these results do not explicitly address the impact of Mn intercalation on the Fermi surface or the topological states of the parent compound, they (a) reveal that the electronic and magnetic states are modified by Mn intercalation and (b) open opportunities for probes such as ARPES to quantify these changes. They also suggest that novel electronic or magnetic behaviors might be induced in this family of materials: e.g. either in the analogues Ti_2Te_2P and Hf_2Te_2P or through chemical substitution of other transition metal ions.

2. Experimental methods

Single crystal specimens of the parent compound were grown using the iodine vapor transport method as previously described [3]. In order to produce the Mn intercalated specimens, an identical process was followed except that Mn was added to the polycrystalline precursor with the ratio 0.25Mn:Zr_2Te_2P. Similar to earlier results, crystals form as hexagonal shaped plates with the *c*-axis perpendicular to the plate. Crystalline structures were determined by XRD measurements and energy dispersive spectroscopy was used to quantify the elemental composition. Powder XRD measurements were done using a Rigaku SmartLab SE x-ray diffractometer with a Cu Kα source and EDS measurements were done using an FEI NOVA 400 nanoSEM scanning electron microscope (SEM) with energy dispersive spectroscopy (EDS) capabilities using an Oxford UItimMAX SDD (silicon drift detector). For single crystal XRD measurements, suitable pieces were cut from larger crystals and were mounted in Dual-Thickness MicroLoopsTM (MiTeGen Loop/Mount) using Parabar oil. Single-crystal XRD data were collected at 200 K, using a Rigaku XtaLAB Synergy-S diffractometer equipped with a HyPix-6000HE Hybrid Photon Counting detector and dual Mo and Cu microfocus sealed x-ray source. Absorption corrections were applied to the data sets using the SADABS program. Data collection and initial cell refinement was conducted using CrysAlis PRO (Agilent, 2013). Final refinements of the structure were performed using SHELXT through the ShelxLE graphical interface package [19–22].

Specimens were prepared for TEM measurements by cutting lamella from a single crystal using focused ion beam in a Thermofisher Scientific DualBeam Helios G4 UC SEM. The single crystal was prealigned using an Enraf-Nonius CAD-4 diffractometer. The TEM sample was studied by atomic resolution high-angle-annular dark field scanning TEM (HAADF-STEM) and elemental composition mapping in a probe-corrected cold emission JEOL JEM-ARM200cF at 200 kV. The imaging resolution is 0.078 nm. The elemental EDS mapping was acquired using oxford Aztec EDS SDD detector. The HAADF-STEM imaging was acquired using a probe 7 cm, and camera length 8 cm, which corresponds to a convergent angle of 21 mrad and a collection inner angle of 74 mrad. TEM sample thickness was measured by electron energy loss spectrum (EELS) via Log-ratio method.

Temperature dependent magnetic susceptibility $\chi(T) = M/H$ measurements were performed at $T = 1.8$–300 K under magnetic fields of $H = 50$ Oe and $H = 5$ kOe applied both parallel ($\parallel$) and perpendicular ($\perp$) to the crystallographic *c* axis using a Quantum Design vibrating sample magnetometer (VSM) Magnetic Property Measurement System. Heat capacity $C(T)$ measurements were performed for $T = 0.4$ K–20 K using the ^{3}He option in Quantum Design Physical Property Measurement System. Normalized electrical resistance $R/R(300\,\mathrm{K})$ measurements were carried out using the four wire method for temperatures $T = 0.4$ K–300 K using the same system. All specimens used for these measurements had lateral dimensions on the order of 2 mm and thickness near 0.1 mm.

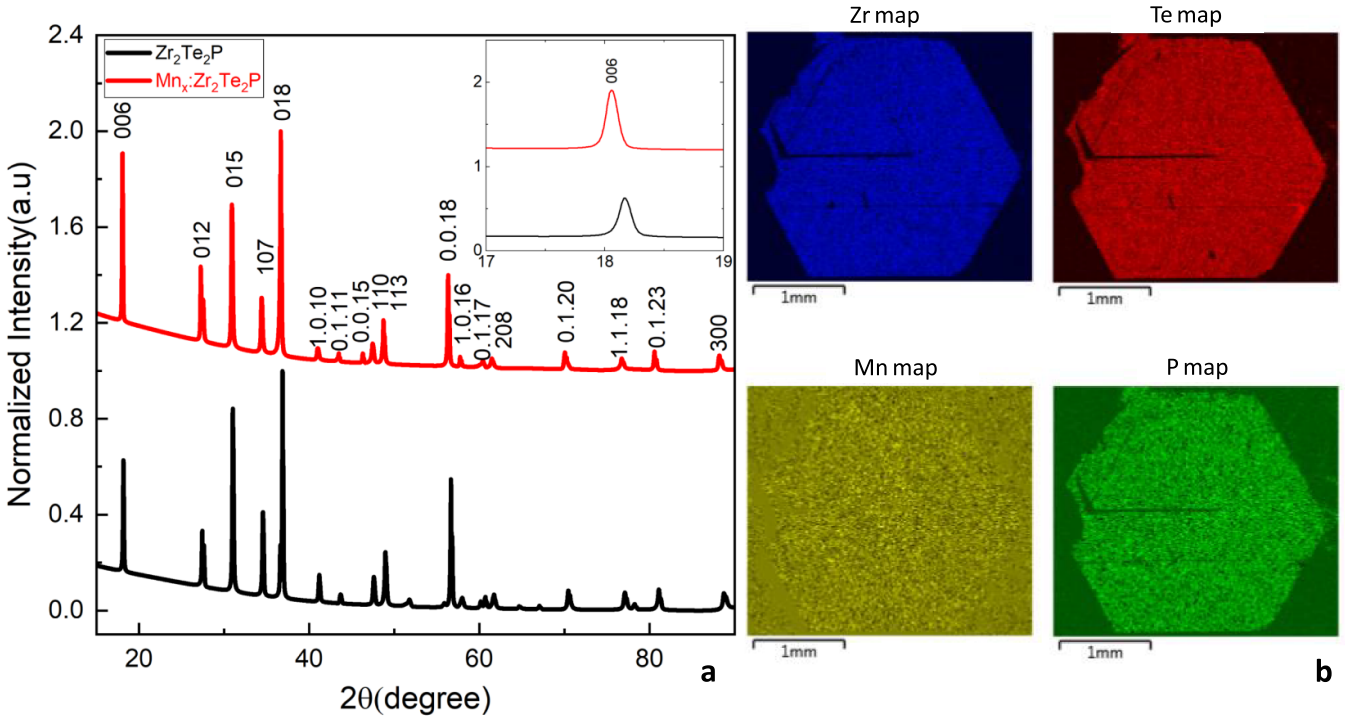

Figure 1. Comparison between the powder XRD patterns of Zr_2Te_2P and Mn_x:Zr_2Te_2P single crystals. (b) Two dimensional energy dispersive spectroscopy data showing the uniform distribution of Zr, Te, P and Mn in the substituted specimens.

3. Crystalline structure and chemical substitution

Results from powder XRD measurements are consistent with earlier reports, and show that Zr_2Te_2P crystallizes in the space group $R\bar{3}m$ (#166) with the lattice parameters $a = 3.8119(3)$ Å and $c = 29.189(3)$ Å ($V = 367.3$ Å^3) [3] (figure 1(a)). The Mn substituted specimens form in the same structure, with only minor changes in the lattice constants; a Rietveld refinement yields $a = 3.778(2)$ Å and $c = 29.191(2)$ Å ($V = 360.8$ Å^3). Semi-quantitative EDS measurements agree with the expected Zr_2Te_2P stoichiometry, and for the chemically substituted samples there is a small amount of Mn distributed uniformly across the crystal (figure 1(b)). The two dimensional EDS maps also show that there is no evidence for inclusions with other stoichiometries. Based on these data we initially find the chemical formulas Zr_2Te_2P and $Mn_{0.06}$:Zr_2Te_2P, although in the latter case it is unclear where the Mn are located.

Single crystal XRD measurements further confirm that the Zr_2Te_2P structures refines in the rhombohedral space group $R\bar{3}m$, and details about the data collection are found in table 1. Importantly, an interstitial site (3b Wyckoff site) between the van der Waals bonded Te–Te layers is identified by analyzing residual electron density peaks on the Fourier difference maps. When assigned as Zr, this site refines to 7% occupied, yielding an overall stoichiometry of $Zr_{0.07}Zr_2Te_2P$. This is consistent with previous reports of $Zr_{2+\delta}Te_2P$ where excess Zr is located within the interstitial layer between the Te–Te ions [18]. For the substituted specimen, the occupancies of all sites were allowed to refine in order to locate the Mn ions. The parent structure sites all refined as being 100% occupied, indicating the Mn is not mixing on these positions. This leaves the partially occupied Zr interstitial site as the most likely position for the Mn ions. The possibility of Mn mixing on this interstitial site is difficult to analyze, given its inherent partial occupancy. Since elemental analysis confirms the incorporation of Mn at 1.2 atomic %, this value was used to fix the Mn occupancy on this 3b Wyckoff site to 6%. The Zr occupancy was

Table 1. Crystallographic data of $Mn_{0.06}Zr_{0.03}Zr_2Te_2P$ compiled from single crystal x-ray diffraction measurements performed at 200 K.

	$Mn_{0.06}Zr_{0.03}Zr_2Te_2P$
Crystal system	rhombohedral
Space group	R-3 m(#166)
a (Å)	3.8266(3)
c (Å)	29.325(3)
Z	3
V (Å^3)	371.88(8)
Density, calc (g cm^{-3})	6.346
Index ranges	$-6 < h < 4, -6 < k < 6,$ $-45 < l < 51$
Reflection collected	1736
Temperature	200 K
Radiation	Mo Kα ($\lambda = 0.7107$Å)
Unique data/parameters	303/12
μ (mm^{-1})	16.054
R1/wR2	0.0337/0.0962
R1/wR2 (all data)	0.0380/0.0967

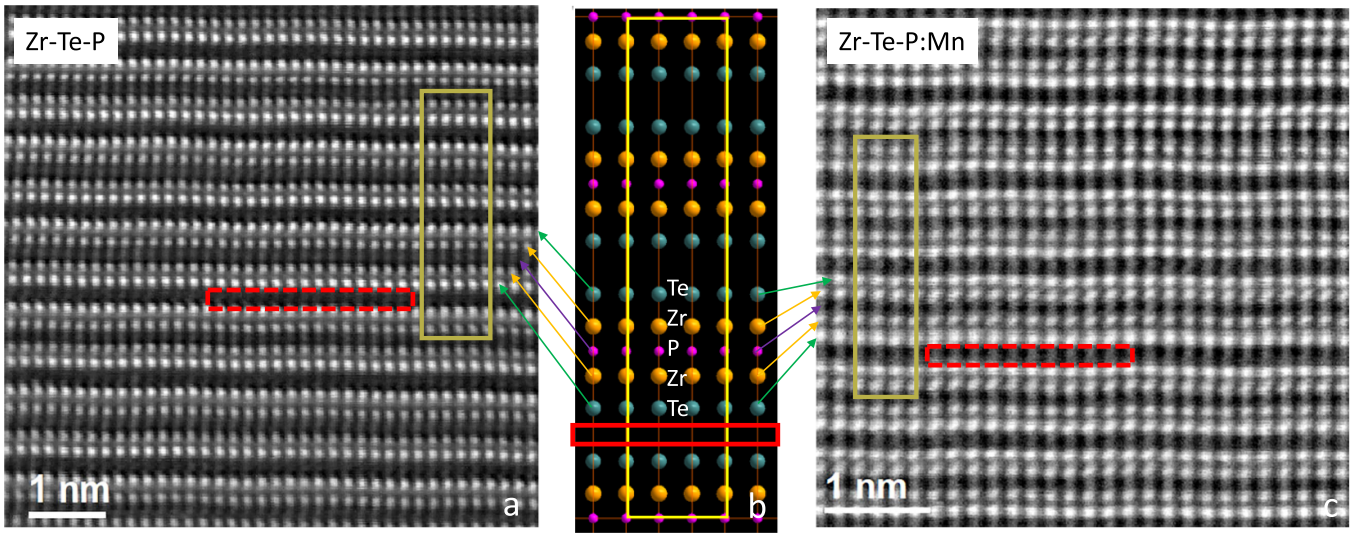

Figure 2. (a) Atomic resolution HAADF-STEM image of the pristine crystal looking down [210]. (b) Schematic of the crystal structure of $Zr_xZr_2Te_2P$. (c) Atomic resolution HAADF-STEM image of the Mn doped crystal looking down [210].

then allowed to vary to account for the total electron density on the site. Refining the site as a Mn/Zr mixed site leads to a Zr occupancy of 3(1)%; i.e. $Mn_{0.06}Zr_{0.03}Zr_2Te_2P$.

In order to further clarify the structures, figures 2(a) and (c) show the atomic resolution HAADF-STEM images for the parent and substituted compounds along the [210] direction. Within the experimental images, the intensity of the atomic columns is proportional to Z^2, where Z is the atomic number [23]: i.e. the atoms that show highest contrast are the Te atomic columns; the medium bright layers are the Zr atomic columns; while P atoms that in between Zr layers have the weakest intensity. For both specimens, this reveals that the atomic structure is well ordered and agrees with XRD measurements. We also find that there is excess electron density between the Te–Te layers (indicated by red boxes) due to the presence of intercalation atoms.

In order to determine the identity of these atoms independently from the XRD measurements, we carried out quantitative image intensity analysis for the parent compound by comparing the theoretical image simulations with the experimental image using the Dr Probe software [24]. In particular, we built a supercell that has the same atomic arrangement as the [210] projected view, with lattice parameters $a = 15.28$ Å, $b = 16.37$ Å, and $c = 6.6$ Å. The atomic column intensity increases with the number of atoms in the column, i.e. with the sample thickness (not shown). For our experiment, the sample thickness was measured to be 28.6 ± 2.4 nm by electron energy loss spectroscopy. However, the sample was prepared by focused-ion-beam milling, which typically produces a thin amorphous surface layer with a thickness of 5–10 nm. Based on this, the estimated thickness of the crystalline sample that was used for this measurement is near 20 nm.

To compare the experimental image intensity with the simulated image intensity, we normalize the image intensity using the equation,

$$I_{\text{image}} = \frac{I_{\text{raw}} - I_{\text{vac}}}{I_{\text{det}} - I_{\text{vac}}} \frac{i_{\text{D}}}{i_{\text{e}}} \tag{1}$$

where I_{raw} is the measured atomic column intensity of the experimental image intensity, I_{det} and I_{vac} are the measured detector intensity and intensity in vacuum, i_{D} is the beam current for detector imaging and i_{e} is the current for sample imaging [25]. By using the Zr column as an internal reference, we find that the simulated image intensity ratio for the P atoms (3*a* Wyckoff site) in between the Zr layers (6*c* Wyckoff site) is $I_P/I_{Zr} = 0.22$ at a thickness of 19.8 nm, which corresponds to 30 P atoms. In order to compare to the experimental image for these sites, the atomic column intensity was determined by integrating the image intensity of an area of 1.31×0.31 Å^2 for the Zr atoms and 0.9×0.9 Å^2 for the P atoms. From this, we find that the experimental averaged intensity ratio for P atoms between the Zr layers is 0.22, which is consistent with simulated intensity. In comparison, the measured intensity ratio for the excess atoms that are found between Te layers is 0.21. The near atomic resolution EDS map excludes the possibility that these excess atoms are phosphorous, making it more likely that they are zirconium. This is consistent with there being 4 to 5 Zr atoms in the extra atomic column and agrees with the sXRD measurements [18]. However, for the chemically substituted specimens, it difficult to locate the Mn ions via these STEM image intensity measurements due to the weak intensity change that results from replacing heavy ions with light ions.

Taken together the XRD and TEM results are understood by considering that Zr_2Te_2P has a layered structure comprised of Te–Zr–P–Zr–Te slabs (with Zr cations coordinated by P and Te anions in slightly distorted octahedra) and a van der Waals gap between the Te layers that is large enough to incorporate interstitial atoms. Previous reports indicate excess Zr incorporates in these interstitial sites, leading to stoichiometries of

$Zr_{2+\delta}Te_2P$ with $0 < \delta < 1.5$ [18]. The very small amount of interstitial Zr indicated by the SC-XRD and TEM measurements is in agreement with the fact that these samples were synthesized without any excess Zr present, and the EDS data does not show an elevated amount of Zr. It is also in agreement with the observed unit cell parameters. Previous studies on the $Zr_{2+\delta}Te_2P$ system with $0 < \delta < 1$ showed a Vegard's law behavior of unit cell parameters with amount of interstitial Zr. In particular, the *c*-axis expanded from 29.35(4) Å (for $\delta = 0$) to 29.70(4) Å (for $\delta = 1$)[18]. The *c*-axis observed in our study (29.325(3) Å) is consistent with the very small amount of interstitial incorporation that we observe experimentally.

4. Magnetism and electronic behavior

Temperature and field dependent magnetization measurements for the Mn substituted specimens are compared to that of the parent compound in figure 3. As shown in panels b and c, the magnetic susceptibility $\chi(T)$ shows paramagnetic behavior at elevated temperatures with easy *ab*-plane anisotropy. Fits to the data using the modified Curie–Weiss expression $\chi(T) = \chi_0 + C/(T-\theta)$ yield the parameters $\chi_0 = -0.000\,24\,\mathrm{cm^3\,mol^{-1}}$, $C = 0.27\,\mathrm{cm^3\,mol^{-1}}$, $\theta = 1.96\,\mathrm{K}$ ($H \parallel c$), and $\theta = -5.63\,\mathrm{K}$ ($H \perp c$). This behavior can be understood as representing a summation of the Pauli paramagnetic component that originates from the $Zr_xZr_2Te_2P$ sublattice ($\chi_0 \approx -0.0001$ was reported previously [2]) and the local moment paramagnetism of the Mn ions. The effective magnetic moment per Mn is calculated from the expression $\mu_{\mathrm{eff}} = 2.82\sqrt{C} = 6.0\ \mu_B$/Mn, which indicates that the Mn ions adopt the divalent state ($\mu_{\mathrm{eff}} = 5.92\ \mu_B/Mn^{2+}$). The θ values also show that there are weak ferromagnetic interactions between the Mn ions in the *ab*-plane and antiferromagnetic interactions along the *c*-axis.

At temperatures below $T \approx 20\,\mathrm{K}$ there is an anisotropic deviation from the Curie–Weiss behavior, which indicates the presence of magnetic fluctuations preceding a magnetically ordered state. For $H \perp c$, this evolves towards ferromagnetic alignment of the spins, as evidenced by the increase in χ that is stronger than the Curie–Weiss behavior, saturation near $T_M \approx 4\,\mathrm{K}$ and hysteretic behavior in low fields for $T < T_M$ (figure 3(d)). As shown in figure 3(e), the hysteresis is removed for $H = 5000$ Oe. In contrast, $\chi(T)$ for $H \parallel c$ shows a weak suppression for $T < T_M$, consistent with there being antiferromagnetic alignment of spins in this direction. Isothermal magnetization curves (figures 3(b)) also reveal a ferromagnetic 's'-shape for $H \perp c$ and a linear evolution for $H \parallel c$. The $H \perp c$ curve extrapolates towards a saturation value $M_s \approx 0.28\mu_B$/F.U., which is consistent with expectations for the partial Mn filling: i.e. $M_s = 5\mu_B/Mn^{2+}$ for a completely filled divalent Mn lattice, whereas our measurement yields $4.6\mu_B$/Mn.

Figure 4 shows the heat capacity divided by temperature C/T for both the parent compound and the substituted specimens. At elevated temperatures, both compounds follow a Fermi liquid temperature dependence given by the expression $C/T = \gamma + \beta T^2$. Fits to the data are shown in figure 4,

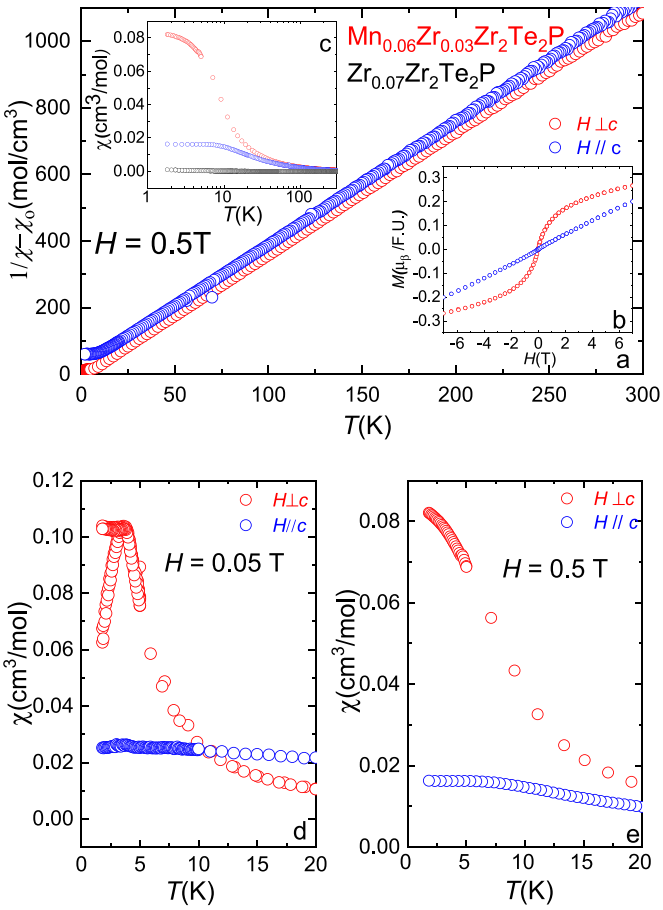

Figure 3. (a) Temperature dependent inverse magnetic susceptibility $(\chi - \chi_0)^{-1}$, where $\chi_0 = -0.000\,24\,\mathrm{cm^3\,mol^{-1}}$ for $Mn_{0.06}Zr_{0.03}Zr_2Te_2P$ (b) Magnetization M versus magnetic field H for temperature T = 1.8 K for magnetic field H applied parallel ∥ and perpendicular ⊥ to the *c*-axis for $Mn_{0.06}Zr_{0.03}Zr_2Te_2P$. (c) Magnetic susceptibility $\chi = M/H$ versus T for $Mn_{0.06}Zr_{0.03}Zr_2Te_2P$ and $Zr_{0.07}Zr_2Te_2P$. (d) Magnetic susceptibility χ = M/H versus T for $H = 50oe$ applied ∥ and ⊥ to the *c*-axis for $Mn_{0.06}Zr_{0.03}Zr_2Te_2P$ (e) Magnetic susceptibility χ = M/H versus T for $H = 5000oe$ applied ∥ and ⊥ to the *c*-axis for $Mn_{0.06}Zr_{0.03}Zr_2Te_2P$.

where, $\beta = 0.58\,\mathrm{mJ\,(mol{\cdot}K^4)^{-1}}$ for both, owing to the fact that the Mn substitution has little impact on the lattice component of the heat capacity. We also find a noteworthy difference in the electronic component of the heat capacity where $\gamma_{Mn} = 36.6\,\mathrm{mJ\,(mol{\cdot}K^2)^{-1}}$ while the parent compound value is $5.28\,\mathrm{mJ\,(mol{\cdot}K^2)^{-1}}$. Given that γ is proportional to the density of states at the Fermi energy for a Fermi liquid, this change suggests that the presence of Mn modifies the Fermi surface. Below $T \approx 15\,\mathrm{K}$ there is also a broad increase in C/T for the Mn compound that can be attributed to spin fluctuations from the Mn moments that begin well above T_M. In order to isolate the Mn contribution to the entropy, the heat capacity of the parent compound is subtracted from that the Mn substituted specimen (figure 4(b)). From this is is seen that C_{mag}/T evolves through a maximum near 4 K, in agreement with the magnetic ordering that is observed in $\chi(T)$. However, this feature does not resolve into a clear second order phase transition, suggesting that disorder plays an important role.

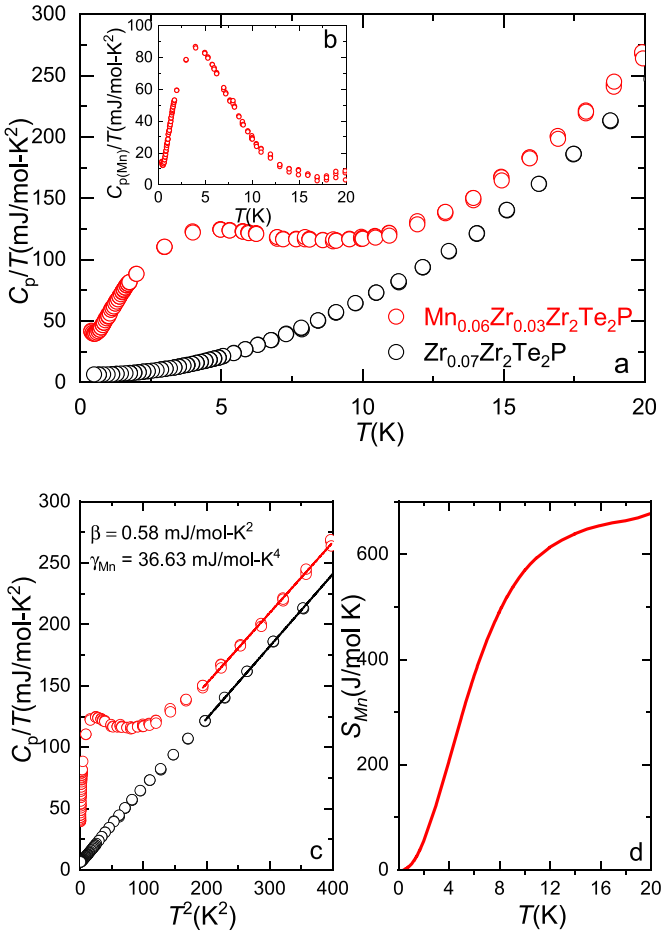

Figure 4. (a) Heat capacity divided by temperature C/T vs T for $Mn_{0.06}Zr_{0.03}Zr_2Te_2P$ and $Zr_{0.07}Zr_2Te_2P$ (b) C/T vs T for Mn ions which was calculated as described in the text. (c) C/T vs T^2 for $Mn_{0.06}Zr_{0.03}Zr_2Te_2P$ and $Zr_{0.07}Zr_2Te_2P$ with a linear fit to the data, representing Fermi liquid. (d) Entropy S of the Mn ions vs T which was calculated as described in the text.

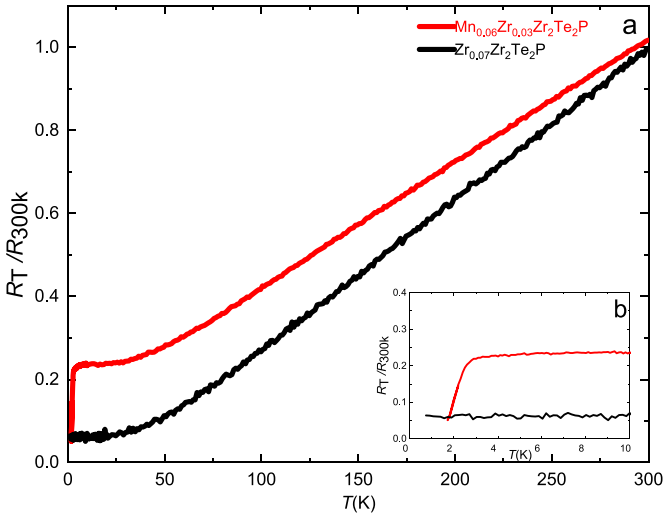

Figure 5. (a) Room temperature normalized electrical resistance R/R_{300k} vs T for both $Zr_{0.07}Zr_2Te_2P$ and $Mn_{0.06}Zr_{0.03}Zr_2Te_2P$. (b) Zoom in at low temperature of room temperature normalized electrical resistance R/R_{300k} vs T.

The resulting curve is then integrated to calculate the magnetic entropy S_{mag} (figure 4(d)), which reaches a value near 0.9 J (mol·K)$^{-1}$ ($S_{Mn} \approx 15$ J (mol·Mn·K)$^{-1}$) at the upper limit of the transition. This value is consistent with expectations for divalent Mn, where $S_{Mn} = 14.9$ J (mol·Mn·K)$^{-1}$ [26–28].

Room temperature normalized electrical resistivity data R/R_{300K} for the Mn substituted and parent compound are compared in figure 5. Both exhibit metallic behavior, but even from room temperature the value of the Mn specimen is enhanced. This suggests the presence of additional scattering mechanisms for the conduction electrons, which could either be attributed to static disorder or scattering though interactions with the Mn d-states. Similar trends extend to low temperatures, where both compounds tend to have saturating values below $T \approx 20$ K but the Mn compound additionally exhibits an abrupt decrease near T_M. This shows that although the ferromagnetic state is disordered, it nonetheless strongly impacts the electronic behavior. Following the transition, the normalized residual resistance reaches values that are similar to that of the parent compound, suggesting that the electronic scattering above T_M is dominated by the Mn ion d-states.

5. Discussion

Our results show that chemical tuning is readily achieved in $Zr_{0.07}Zr_2Te_2P$ at levels that are comparable to the binary topological insulator analogues $Bi_2(Se,Te)_3$ [26]. This was earlier seen for Cu_x:Zr_2Te_2P [1] and now is shown for $Mn_{0.06}Zr_{0.03}Zr_2Te_2P$, where the presence of additional Zr ions between the Te–Te layers suggests that a reexamination of earlier electronic band structure calculations [3] may provide additional insights into previous results. Given that Mn and Cu are located on opposite extremes of the transition metal series, it appears that it will be possible to substitute many other d-electron elements into this structure and the related compounds Ti_2Te_2P and Hf_2Te_2P. This also invites efforts to modify the growth conditions to increase the intercalant concentrations.

In the particular case of $Mn_{0.06}Zr_{0.03}Zr_2Te_2P$, we find that the Mn ions adopt a divalent electronic shell configuration, as evidenced by Curie–Weiss behavior that is seen in the magnetic susceptibility, the saturation magnetic moment, and the magnetic entropy. The Mn ions appear to be randomly distributed within the Te–Te layers, with their density being sufficient to support magnetic interactions that are likely mediated through the Ruderman–Kittel–Kasuya–Yosida interaction [29–31]. This results in a ferromagnetic exchange within the ab-plane and an antiferromagnetic interaction along the c-axis, culminating in magnetic order at $T_M \approx 4$ K. These results are similar to what is seen when Mn is introduced into $Bi_2(Se,Te)_3$, where ferromagnetic ordering is seen at similar concentrations [26].

We also find that the introduction of Mn impacts the electronic state, as seen in the enhanced value of the electronic coefficient of the heat capacity γ_{Mn}. From a naive perspective, this might indicate that the charge carrier masses are enhanced (e.g. through *s–d* hybridization [32, 33]), but it is unclear is whether it might instead be due to charge doping which repositions the Fermi energy into a region of the band structure with a larger density of states. Further studies that directly assess the Fermi surface topography and the charge carrier effective masses (quantum oscillation or ARPES measurements) will be needed to clarify this point and are key factors as we move forward towards understanding the evolution of the electronic state in this material. It is also seen that the Mn ions modify the electrical transport, although it is not yet clear whether any part of this relates to modification of the nontrivial electronic bands. In principle, the divalent Mn ions introduce time reversal symmetry breaking that would split the Dirac bands into Weyl points [34, 35]. This might induce novel topological behavior, but we note that there also are many conventional bands to consider and it is not yet clear whether the Fermi energy is substantially moved in these specimens. Further work to investigate the magnetoresistance and to search for an anomalous quantum Hall effect will be useful to clarify this point.

6. Conclusion

We have reported results for Mn substituted Zr_2Te_2P, where measurements show that it crystallizes in the expected tetradymite structure with Mn randomly positioned in the interstitial sites between the tellurium layers. Single crystal XRD and TEM measurements also reveal that, even for the parent compound, the Te–Te layers are partially filled by Zr. Based on this, we propose the chemical formulas $Zr_{0.07}Zr_2Te_2P$ and $Mn_{0.06}Zr_{0.03}Zr_2Te_2P$. For the substituted specimens, the Mn ions are found to be in the divalent state, which produces anisotropic Curie–Weiss behavior that culminates in disordered magnetic order seen in the magnetic, heat capacity, and electrical transport. This transition is not a simple long range ordering and additional studies such as neutron scattering are needed to further clarify the role of disorder. Similar to the parent compound, heat capacity and electrical transport measurements show metallic behavior, but the electronic coefficient of the heat capacity ($\gamma_{Mn} \approx 36.6\,\mathrm{mJ\,(mol{\cdot}K^2)^{-1}}$) is strongly enhanced. Based on this, we conclude that Mn substitution simultaneously introduces magnetic interactions and tunes the electronic state. This opens a path towards inducing novel behavior in Zr_2Te_2P and the broader family of ternary tetradymite materials.

Data availability statement

The data that support the findings of this study are available upon reasonable request from the authors.

Acknowledgments

R B, O O, and K F were supported by the National Science Foundation through NSF DMR-1904361. S E L and J W H were supported by the National Science Foundation through NSF DMR-21-26077. The National High Magnetic Field Laboratory is supported by the National Science Foundation through NSF DMR-1644779 and State of Florida.

ORCID iDs

O Oladehin https://orcid.org/0000-0002-1732-0620
R E Baumbach https://orcid.org/0000-0002-6314-3629

References

[1] Ji H, Pletikosić I S, Gibson Q D, Sahasrabudhe G, Valla T and Cava R J 2016 Strong topological metal material with multiple Dirac cones *Phys. Rev.* B **93** 045315
[2] Chen K-W, Das S, Rhodes D, Memaran S, Besara T, Siegrist T, Manousakis E, Balicas L and Baumbach R E 2016 Uncovering the behavior of Hf_2Te_2P and the candidate Dirac metal Zr_2Te_2P *J. Phys.: Condens. Matter* **28** 14LT01
[3] Chen K-W *et al* 2018 Converting topological insulators into topological metals within the tetradymite family *Phys. Rev.* B **97** 165112
[4] Hosen M M *et al* 2018 Distinct multiple fermionic states in a single topological metal *Nat. Commun.* **9** 3002
[5] Boyle T J *et al* 2019 Topological surface states above the Fermi level in Hf_2Te_2P *Phys. Rev.* B **100** 081105
[6] Dai J *et al* 2021 Experimental observation and spin texture of Dirac node arcs in tetradymite topological metals *Phys. Rev. Lett.* **126** 196407
[7] Hor Y S, Williams A J, Checkelsky J G, Roushan P, Seo J, Xu Q, Zandbergen H W, Yazdani A, Ong N P and Cava R J 2010 Superconductivity in $Cu_xBi_2Se_3$ and its implications for pairing in the undoped topological insulator *Phys. Rev. Lett.* **104** 057001
[8] Li Z J, Liu Y, White S C, Wahl P, Xie X M, Jiang M H and Lin C T 2012 Single crystal growth and transport properties of Cu-doped topological insulator Bi_2Se_3 *Phys. Proc.* **36** 638–43
[9] Fang Y, You W-L and Li M 2020 Unconventional superconductivity in $Cu_xBi_2Se_3$ from magnetic susceptibility and electrical transport *New J. Phys.* **22** 053026
[10] Kong P P *et al* 2013 Superconductivity of the topological insulator Bi_2Se_3 at high pressure *J. Phys.: Condens. Matter* **25** 362204
[11] Liu Z, Yao X, Shao J, Zuo M, Pi Li, Tan S, Zhang C and Zhang Y 2015 Superconductivity with topological surface state in $Sr_xBi_2Se_3$ *J. Am. Chem. Soc.* **137** 10512–5
[12] Han C Q *et al* 2015 Electronic structure of a superconducting topological insulator Sr-doped Bi_2Se_3 *Appl. Phys. Lett.* **107** 171602
[13] Ju L, Xu T-S, Hu D, Cui H-T, Zhang Y-J and Shi C-M 2015 Transition metal substitutions induce ferromagnetism in Bi_2Te_3 *Chin. J. Chem. Phys.* **28** 173–8
[14] Zhang J-M, Ming W, Huang Z, Liu G-B, Kou X, Fan Y, Wang K L and Yao Y 2013 Stability, electronic and magnetic properties of the magnetically doped topological insulators Bi_2Se_3, Bi_2Te_3 and Sb_2Te_3 *Phys. Rev.* B **88** 235131

[15] Ptok A, Kapcia K J and Ciechan A 2020 Electronic properties of Bi_2Se_3 dopped by 3d transition metal (Mn, Fe, Co, or Ni) ions *J. Phys.: Condens. Matter* **33** 065501
[16] Liu C, Zang Y, Ruan W, Gong Y, He K, Ma X, Xue Q-K and Wang Y 2017 Dimensional crossover-induced topological Hall effect in a magnetic topological insulator *Phys. Rev. Lett.* **119** 176809
[17] Wang Y *et al* 2019 Magnetic anisotropy and topological Hall effect in the trigonal chromium tellurides Cr_5Te_8 *Phys. Rev.* B **100** 024434
[18] Tschulik K, Hoffmann S, Fokwa B P T, Gilleßen M and Schmidt P 2010 Studies regarding the homogeneity range of the zirconium phosphide telluride $Zr_{2+\delta}PTe_2$ *Solid State Sci.* **12** 2030–5
[19] CrysAlis PRO Agilent and PRO CrysAlis 2014 Agilent Technologies Ltd. Yarnton, Oxfordshire, England
[20] Sheldrick G M 2008 A short history of *SHELX Acta Crystallogr.* A **64** 112–22
[21] Sheldrick G M 2015 Crystal structure refinement with *SHELXL Acta Crystallogr.* C **71** 3–8
[22] Hübschle C B, Sheldrick G M and Dittrich B 2011 *ShelXle*: a Qt graphical user interface for *SHELXL J. Appl. Crystallogr.* **44** 1281–4
[23] Pennycook S J and Boatner L A 1988 Chemically sensitive structure-imaging with a scanning transmission electron microscope *Nature* **336** 565–7
[24] Barthel J 2018 Dr. Probe: a software for high-resolution STEM image simulation *Ultramicroscopy* **193** 1–11
[25] MacAuthor K E 2015 *PhD Thesis* Trinity College, University of Oxford
[26] Hor Y S *et al* 2010 Development of ferromagnetism in the doped topological insulator Bi_{2-x} Mn_xTe_3 *Phys. Rev.* B **81** 195203
[27] Maurya V K, Yadav P K and Patnaik S 2015 Anti-ferromagnetism through Mn doping in topological insulator Bi_2Se_3 *AIP Conf. Proc.* **1665** 130041
[28] Watson M D *et al* 2013 Study of the structural, electric and magnetic properties of Mn-doped Bi_2Te_3 single crystals *New J. Phys.* **15** 103016
[29] Kasuya T 1956 A theory of metallic ferro-and antiferromagnetism on Zener's model *Prog. Theor. Phys.* **16** 45–57
[30] Yosida K 1957 Magnetic properties of Cu-Mn alloys *Phys. Rev.* **106** 893
[31] Indirect exchange coupling of nuclear magnetic moments by conduction electrons
[32] Tanaka S, Shimazui N, Takatsu H, Yonezawa S and Maeno Y 2009 Heavy-mass behavior of ordered perovskites $ACu_3Ru_4O_12$ (A= Na, Ca, La) *J. Phys. Soc. Japan* **78** 024706
[33] Kato H, Tsuruta T, Nishioka T, Matsumura M, Sakai H and Kambe S 2007 A Cu NQR study in a d-electron heavy-fermion system, $CaCu_3Ru_4O_{12}$ *J. Phys. Chem. Solids* **68** 2187–90
[34] Lin Z *et al* 2020 Dirac fermions in antiferromagnetic FeSn kagome lattices with combined space inversion and time-reversal symmetry *Phys. Rev.* B **102** 155103
[35] Gorbar E V, Miransky V A, Shovkovy I A and Sukhachov P O 2015 Dirac semimetals A_3Bi(A = Na, K, Rb) as $\mathbb{Z}_2$ Weyl semimetals *Phys. Rev.* B **91** 121101